SCIENTIFIC REP✺RTS

OPEN

Field Effect Transistor Based on Layered NiPS₃

Ramesh Naidu Jenjeti, Rajat Kumar, Muthu P. Austeria & S. Sampath

Layered metal phosphochalcogenides of molecular formula, MPX_3 (M = Mn, Fe, Co, Ni, etc and X = S, Se) have been emerging as new class of semiconductors towards various catalytic and optoelectronic applications. The low cleavage energy associated with these layered chalcogenides may lead to devices with very thin semiconductor channels. Herein, we report the first successful fabrication of field effect transistor (FET) using layered $NiPS_3$ that reveals n-type semiconducting behavior. Devices using bulk and few-layer $NiPS_3$ with gold contacts show on/off ratios of $\sim 10^3$–10^5 at 25 °C. The device characteristics reveal an increase in on-state current with decrease in threshold voltage and the Schottky barrier height is extracted to be 112 meV. Density functional theory calculations reveal various parameters that affect electron/hole doping in the layered phosphochalcogenide material.

Among the 2-dimensional layered materials, graphene has received considerable attention due to its ultrahigh mobility and tunability of layer thickness[1,2]. However, the zero band gap of pristine graphene limits its use in optoelectronics and other applications. Transition metal dichalcogenides (TMDs) such as MoS_2 form the next class of well-studied compounds with certain band gap tunability[3–12]. Bulk MoS_2 is semiconducting in nature with an indirect band gap of ~ 1.2–1.4 eV[13], while mono-layer MoS_2 possesses direct band gap of 1.8 eV[14]. This has led to various fundamental studies in the areas of electronic, optoelectronic and ultrasensitive sensors with atomically thin MoS_2 membranes[15–23]. Though the TMDs (MoS_2, WSe_2) have shown high on/off ratios with tunable band gap in the visible wavelength range[24,25], the low carrier mobility is of concern. Recently, phosphorene has been looked at, as a potential candidate for optoelectronic, electronic devices and sensors[26–28], owing to its high on/off ratio coupled with high carrier mobility[29,30]. The disadvantage though is its stability that is still being tackled. Both TMDs and black phosphorus possess small band gaps thus restricting their applications in optoelectronics using light of short wavelength field effect transistors (FETs)[20,26].

Continuous search for new 2D-materials has recently led to a well-studied class of bulk layered semiconducting metal phosphotrichalcogenides with formula MPX_3 (M = Ni, Fe, Mn, Co, V, Zn etc; X = S and Se). This class of layered compounds have been wellexplored in the latter half of 20th century towards understanding their crystal structure and intercalation properties[31–39]. However, little is known as for as few layer MPX_3 materials are concerned and recently, this area has been attracting considerable attention[40–42] particularly towards catalysis[43–47] and UV photodetector[48]. A recent review[49] highlights the importance of this class of materials and their multi-functionality. The MPX_3 family of materials possesses wide variation of band gap values from 1.3 eV to 3.5 eV. The cleavage energy of MPX_3 is reported to similar and in certain cases, lower than that of graphene and TMDs[41,50]. Depending on the nature of metal ion, MPX_3 family of compounds may open up ways to fabricate field effect transistors which is still a missing link in the current literature. A recent report on the first principle calculations on $MnPSe_3$ reveals transformation from anti-ferromagnetic semiconductor to ferromagnetic half-metal by carrier doping[37]. Raman spectroscopic studies on certain stable MPX_3 compounds has been recently reported[40,41]. However, electronic devices based on these classes of materials such as field effect transistors have not been explored in the literature so far.

Among the MPX_3 family of semiconductors, $NiPS_3$ is a layered ternary metal thiophosphate with monoclinic crystal system containing two molecular formula units per unit cell ($Ni_2P_2S_6$), with point group, C2/m. $NiPS_3$ is comprised of layers of covalently bonded units of $(P_2S_6)^{4-}$ bipyramids with honeycomb arrangement of divalent nickel ions. The sulfur atoms are hexagonally arranged along the c-axis in ABCABC sequence. The inter layers are connected through weak van der Waals forces similar to other layered 2D-materials such as TMDs. Hence, it is possible to separate the layers by mechanical exfoliation. Bulk $NiPS_3$ is anti-ferromagnetic with magnetic moment of 3.9 BM[51]. The reported band gap of bulk $NiPS_3$ is ~ 1.6 eV[43].

Department of Inorganic and Physical Chemistry, Indian Institute of Science, Bangalore, 560012, India. Correspondence and requests for materials should be addressed to M.P.A. (email: muthu.austeria@gmail.com) or S.S. (email: sampath@iisc.ac.in)
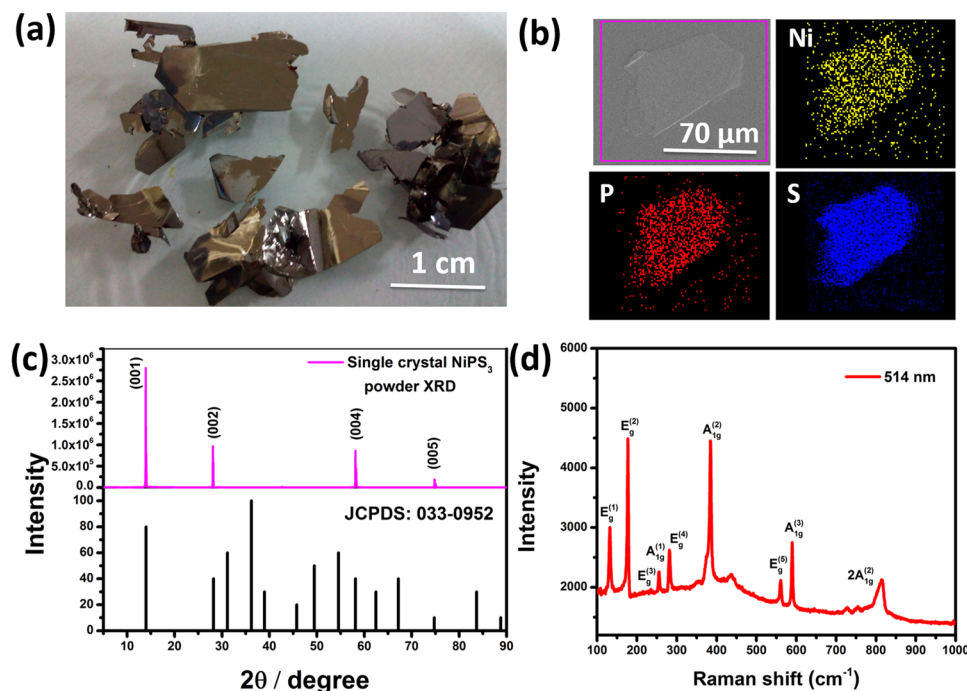
Figure 1. (**a**) Photographic images of $NiPS_3$ crystals. (**b**) Scanning electron microscopic image with elemental mapping of mechanically exfoliated few layer $NiPS_3$ on Si/SiO_2 along with (**c**). XRD pattern of the bulk crystals and the corresponding standard pattern. (**d**) Raman spectrum of $NiPS_3$ crystals obtained with 514 nm excitation laser.

In the present study, we have synthesized fairly large sized, oriented crystals of $NiPS_3$ using a high temperature solid state method and explored its use in FETs. The material is thoroughly characterized using X-ray diffraction (XRD), Raman spectroscopy, transmission electron microscopy (TEM) and atomic force microscopy (AFM). Field effect transistors (FETs) have been fabricated and temperature dependent electrical transport measurements have been carried out. Density functional theory (DFT) calculations reveal the possible parameters that help understand the carrier-type observed in the electrical transport studies.

Result and Discussion

Highly oriented crystals of $NiPS_3$ obtained in the present study are shiny black in colour with high crystallinity and the X-ray diffraction pattern shows very high orientation in the $(00l)$ direction. Figure 1(a–c) shows the optical images, scanning electron microscopic image with elemental mapping and the XRD pattern of large sized crystals. The Raman spectrum of the bulk material (Fig. 1d) shows a band at $253\,cm^{-1}$ which is assigned to the $A_{1g}^{(1)}$ mode. The high intense peak at $176\,cm^{-1}$ is due $E_g^{(2)}$ vibration and the one observed at $384\,cm^{-1}$ is due to symmetric stretching vibration of P-S bond in the P_2S_6 units (assigned as $A_{1g}^{(2)}$). The bands at $236\,cm^{-1}$, $280\,cm^{-1}$, $560\,cm^{-1}$ and $588\,cm^{-1}$ are assigned to $E_g^{(3)}$, $E_g^{(4)}$, $E_g^{(5)}$ and $A_{1g}^{(3)}$ modes[40,51,52]. The bulk electrical conductivity has been measured to be 1.64×10^{-7} S/cm at 25 °C. TMDs such as 2H MoS_2, $MoSe_2$, WSe_2 and $MoTe_2$ show values of 3×10^{-2}, 2×10^{-1}, 6 and 1.8 S/cm respectively at 25 °C[53].

The trans conductance (g_m) value of $NiPS_3$ obtained from the fabricated FET devices is 2.5 µS/cm. The TMDs, on the other hand show values of 0.5–3 µS/µm for back-gated devices[16]. The morphology and microstructure of exfoliated $NiPS_3$ nanosheets are given in Fig. 2. Spatially resolved EDS elemental mapping of Ni, P and S elements reveals a ratio of 1:1:3 as expected with uniform distribution of the elements obtained over the entire surface. The HRTEM image shows well-resolved lattice fringes along (002) plane, confirming the quality of the crystalline nanosheet (Fig. 2b). The selected area electron diffraction (SAED) pattern displays a single set of diffraction spots, further confirming the oriented nature of the exfoliated nanosheets (Fig. 2c).

The low cleavage energy[41] reported for $NiPS_3$ makes it possible to fabricate devices containing few to several layers of the material. The bulk crystals are exfoliated by mechanical means (Fig. S2) as reported for graphene-based materials[54]. The devices used in the present study are prepared by transferring the material onto pre-fabricated contact pads on highly doped silicon as the back gate with 230 nm SiO_2 dielectric by standard mechanical exfoliation method using scotch tape. The source-drain metal contacts are given using 10/60 nm ITO/Au. The flakes in the devices have been characterized using optical microscopy, Raman spectroscopy (with excitation wave length of 514 nm) and the thickness is measured using atomic force microscopy (AFM). Several micron-sized, large flakes with thicknesses ranging from 1.5–10 nm have been achieved in the devices. The characteristics discussed the present study are for devices with varying thicknesses of 1.5–60 nm consisting of 2–75 layers.
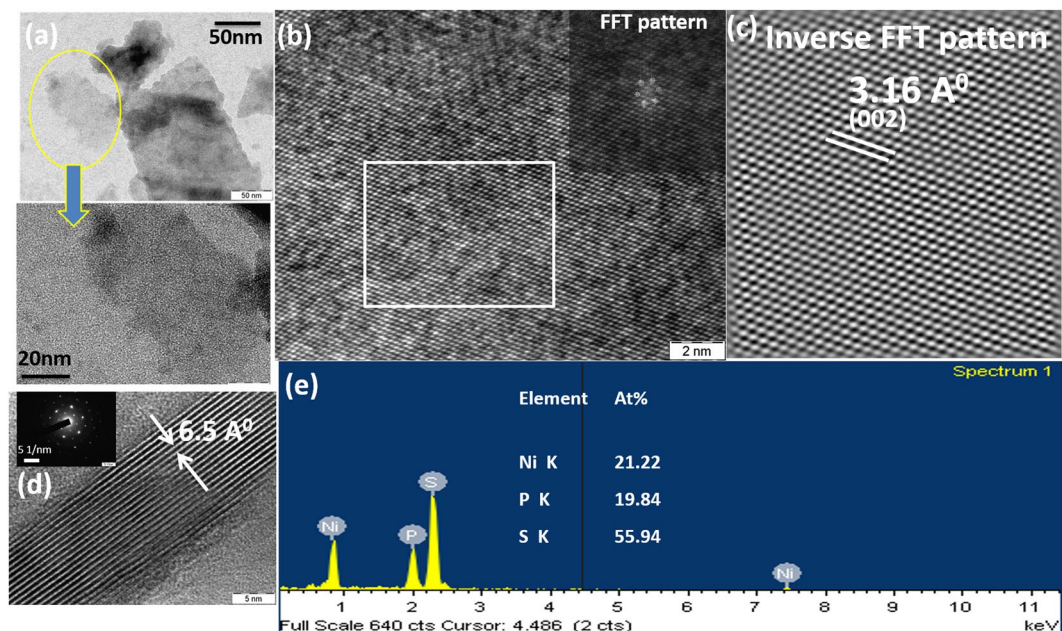
Figure 2. (**a,b,d**) High resolution TEM images of mechanically exfoliated few-layer NiPS$_3$ showing an interlayer spacing of 6.5 Å and the corresponding (**c**) FFT and (**e**) EDS mapping show the elemental ratio of Ni, P and S to be ~1:1:3.
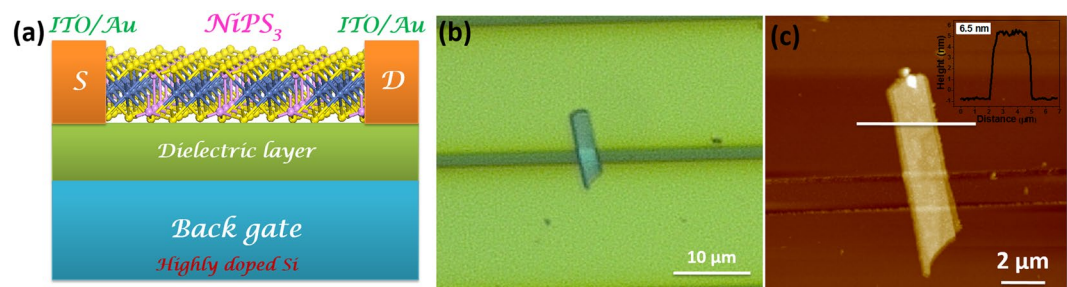

Figure 3. (**a**) Schematic of few-layer NiPS$_3$ field effect transistor. (**b**) Optical micrograph of a typical NiPS$_3$ device. (**c**) Atomic force microscopic image of 6.5 nm NiPS$_3$ flake on Si/SiO$_2$ with ITO/Au contact pads and the corresponding height profile measured across NiPS$_3$ flake.

The back gated field effect transistors (FETs) have been fabricated and the characteristics followed. The data given below (Fig. 3) is for a channel length of 2.5 μm. The schematic of the FET along with the optical image, AFM picture and the height profile are shown in Fig. 3. It is clear that a large size single flake is present within the channel and the height is measured to be ~6.5 nm. This corresponds to 6 to 8 layers based on the single layer thickness of around 8 to 11 Å[40]. Standard transistor measurements have been carried out in vacuum (~10^{-5} mbar) and to ensure reproducibility, we have carried out measurements using several tens to hundreds of different devices.

The on-off ratio, threshold voltage, carrier type and mobility have been evaluated. The output characteristics of the devices, source-drain voltage (V$_{ds}$) vs. source-drain current (I$_{ds}$) at different gate voltages are shown in Fig. 4. The non-linear behavior possibly arises due to the schottky barrier contact with Au metal. The current increases with increasing positive gate voltage, suggesting n-type semiconducting behavior. The on-off ratio estimated based on the transfer characteristics is ~10^3–10^5 for most of the devices (Fig. 5) at 25 °C. The field effect mobility is extracted from the I$_{ds}$-V$_{bg}$ curve using the following expression[5].

$$\mu = \left[\frac{dI_{ds}}{dV_{ds}}\right] \times \left[\frac{L}{WC_iV_{ds}}\right]$$

(1)

where μ is the mobility, W (3 μm) is the channel width, L (2.5 μm) is the channel length and C$_i$ (1.5 × 10^{-4} F/m^2) is the capacitance between the channel and the back gate per unit area (C$_i$ = ε$_o$ε$_r$/d; ε$_o$ = 8.85 × 10^{-12} F·m^{-1}; ε$_r$ = 3.9; d = 230 nm). The mobility values are determined to be ~0.5–1 cm^2/Vs. It is low as compared to several devices known in the literature. However, it is possible that poor contact with the metal electrode may be responsible as reported for MoS$_2$ and WSe$_2$[55,56]. The mobility may be improved further by using high-K dielectric materials in top gated devices and is being presently studied.
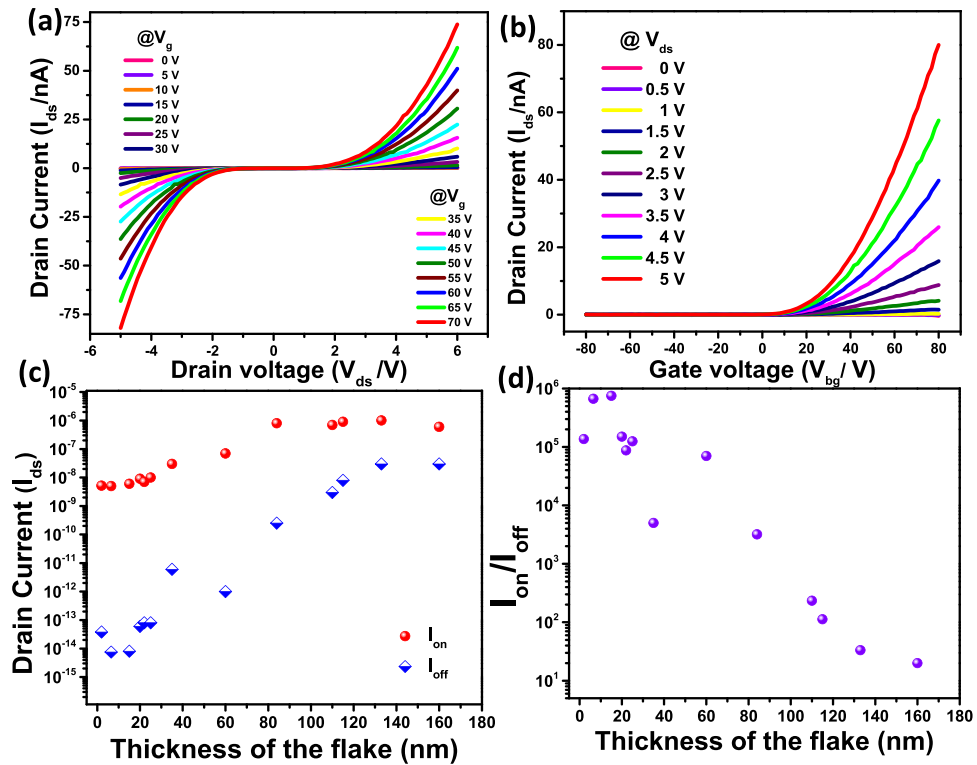
Figure 4. Electronic properties of few-layer NiPS$_3$. (**a**) Drain current versus drain voltage for various Vg values as given in the figure, at 25 °C. (**b**) Drain current verses back gate voltage for V$_{ds}$ ranging from 0 to 5 V. The FET characteristics obtained for a flake thickness of 6.5 nm NiPS$_3$. (**c**) Thickness dependent I$_{on}$ (red) and I$_{off}$ (blue) currents. (**d**) Thickness dependence of I$_{on}$/I$_{off}$ ratio.
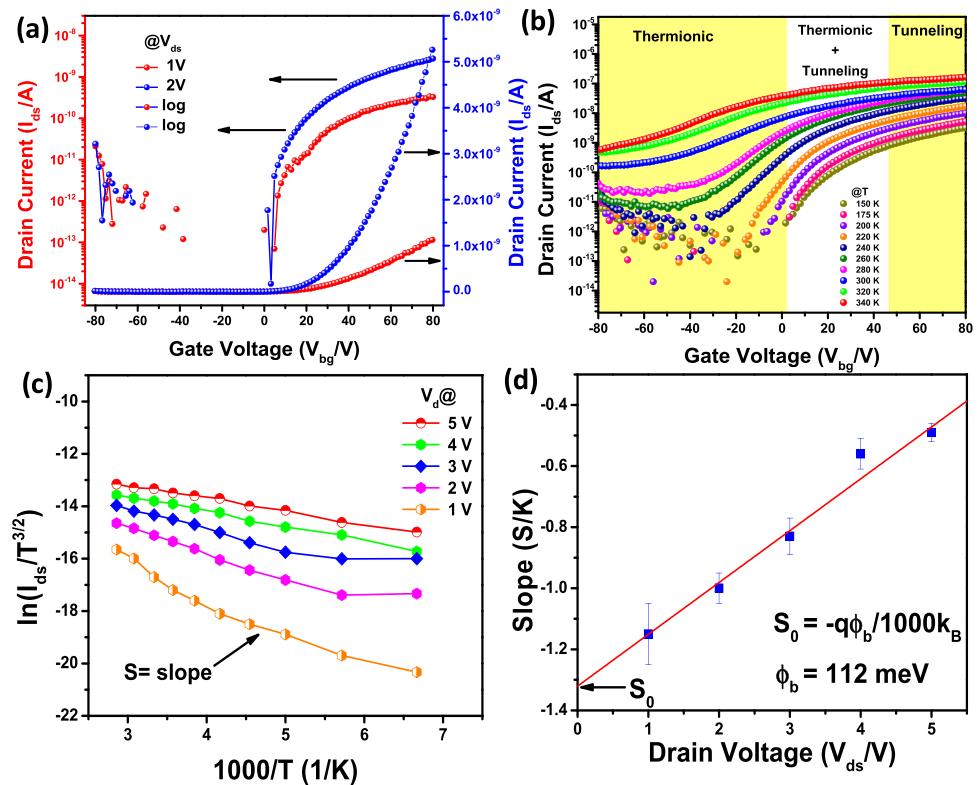

Figure 5. (**a**) Source-drain current as a function of gate voltage. (**b**) Temperature dependent transfer characteristics of the device. (**c**) Arrehenius plots of $\ln(I_{ds}/T^{3/2})$ vs 1000/T. (**d**) Slope extracted from Fig. 5c as a function of V$_{ds}$. Φ_B is derived from the y-intercept, S$_0$.

A threshold voltage of 10 V is estimated by extrapolating the transfer characteristics. The I_{on}/I_{off} ratio as a function of thickness of the material is shown in Fig. 4d and it is observed that for thicknesses less than 60 nm, the I_{on}/I_{off} ~ 10^5 and it is of the order of 10^4–10^2 when the thickness is in the range 60–100 nm. Further increase in thickness leads to small I_{on}/I_{off} ratio. This indirectly points to depletion length of ~100 nm for the present device. The I_{on}/I_{off} ratio for MoS_2 has been reported to be in the range of 10^7–10^1 for thicknesses varying from few nm to 250 nm[57]. The relationship between the depletion length with various parameters of the material is given below (Equation 2),

$$W_{max} = \sqrt{\frac{4kT\varepsilon_s\varepsilon_r}{q^2N_d}\ln\frac{N_d}{n_i}}$$

(2)

where, k is the Boltzmann constant, T is absolute temperature, q is elementary charge, ε_r is the vacuum permittivity, ε_s is the relative dielectric constant of $NiPS_3$ (~9.2)[58], n_i is intrinsic carrier concentration 6×10^5 cm^{-3}, and N_d is unintentional doping level. $NiPS_3$ is known to be an intrinsic semiconductor with low conductivity[59]. For a depletion length of ~100 nm, the N_d works out to be 1.5×10^{17} cm^{-3} that points to certain level of doping in the material. It should be noted that $NiPS_3$ possesses $[P_2S_6]^{4-}$ clusters that leads to 'ionic' interactions with Ni^{2+} in the material[60]. The contributions of thermionic emission current component ($I_{thermionic}$) and the thermally assisted tunneling current component ($I_{tunneling}$) under different gate voltages indicate band bending at the metal - semiconductor interface. The Schottky barrier height (SBH) at the interface has been determined based on thermionic emission model using temperature dependent transport behavior. Figure 5b shows the device characteristics at different temperatures and the change in current with the gate voltages is plotted (Fig. 5c) to extract the SBH using the following relationship (Equation 3).

$$I_{ds} = AA^*T^{3/2}e^{\left[-\frac{q}{kBT}\left(\Phi B - \frac{V_{ds}}{n}\right)\right]}$$

(3)

where A is contact area of the junction, A* is the Richardson constant, q is magnitude of electron charge, Φ_B is the Schottky barrier height, k_B is Boltzmann constant, n is ideality factor, V_{ds} is drain-source voltage and T is the temperature. For the device shown in Fig. 3, the values of $\ln(I_{ds}/T^{3/2})$ are plotted against 1000/T at different V_{ds} as shown in Fig. 5c. The slope at each bias is determined and plotted as a function of source-drain bias as shown in Fig. 5d. The intercept observed in Fig. 5b is determined (S_0). Using the equation 4,

$$S_0 = -\frac{q\Phi B}{1000K_B}$$

(4)

the Schottky barrier height is calculated to be 112 meV for the 8 layer device of $NiPS_3$. This value is similar to that observed for transition metal chalcogenide based devices[21,61]. Based on the small SBH determined from the transfer behavior, it may be expected that FET would show n-type unipolar behaviour and consequently the barrier height for holes is high [(band gap − SBH) for electrons].

FET devices based on bi-layer and bulk NiPS₃. The output characteristics of the bi-layer $NiPS_3$ device, source-drain voltage (V_{ds}) vs. source-drain current (I_{ds}) at different gate voltages are shown in Fig. S3. The current amplitude increases with increasing positive gate voltage as observed for the n-type behavior of eight-layer device. However, the current values for the bi-layer $NiPS_3$ device are quite low as compared to the multilayer device. It has been reported by Kim and co-workers[62] that density of states for multilayer MoS_2 is several times larger than that of single layer MoS_2 thus making multilayers attractive for device applications with considerable drain currents. The on-off ratio estimated based on the transfer characteristics is ~10^5 for the bi-layer devices and the mobility has been estimated to be ~0.5 cm²/Vs. The variation of mobility as a function of thickness of the flake (Fig. S4) is similar to the observations on reported TMD-based devices[63]. This is possibly due to scattering caused by extrinsic charge impurity that decreases as the number of layers increases, as reported for MoS_2[63]. The transport behavior for the device with 60 nm thick flake (Fig. S5) is similar to that observed for other thicknesses. The current values are large with on-off ratio and mobility of ~10^2–10^3 and ~3.5 cm²/Vs respectively.

DFT studies. Density functional theory (DFT) calculations have been performed to decipher the electrical transport behavior of $NiPS_3$. The crystal structure of $NiPS_3$ (Fig. 6a) illustrates that the $(P_2S_6)^{4-}$ units are in staggered configuration where all sulphur atoms are coordinated to Ni in distorted octahedral environment and the van der Waals interlayer distance between S…S is 4.422 Å. The optimized geometry illustrates that the $(P_2S_6)^{4-}$ units show dihedral (angle involving S-P-P-S structure) angle of 180°. The six S-P-P angles in the $(P_2S_6)^{4-}$ unit being almost equal (Table S1), reveals that there is no strain present in the P_2S_6 clusters even when Ni is present in the lattice (Fig. 6b). On the contrary, the NiS_6^{10-} units clearly reveal distortions in the structure. The distortion parameters (distortion angle, denoted as σ^2oct)[64–66] are measured as proposed by Robinson et al.[67]. Based on the structure (Fig. 6c), it is seen that there are twelve different bond angles that can be measured and the values are given in the Supporting Information (Table S1). The average σ^2oct determined for neutral $NiPS_3$ is 26.02°.

The DOS calculations (Fig. S6a) confirm the presence of up and down spins in the frontier region. The atom projected DOS given in Figure S7 indicates that the 3d bands of Ni (spin-up) are well-mixed with the 3p bands of S confirming strong hybridization as shown in SI (Fig. S6b,d). The upper valence bands are comprised of 3d orbital of Ni and 3p orbital of S. Sulphur dominates the valance band region whereas nickel contribution is maximum at the conduction band region. The orbital projected DOS of individual atoms reveals the presence of large population of 3p orbital of S at the Fermi whereas the contribution by phosphorus is very minimum. This may be due to the strong P-P covalent bond that appears in the lower valence band (−5 to −7 eV) energy region (Fig. S6c).
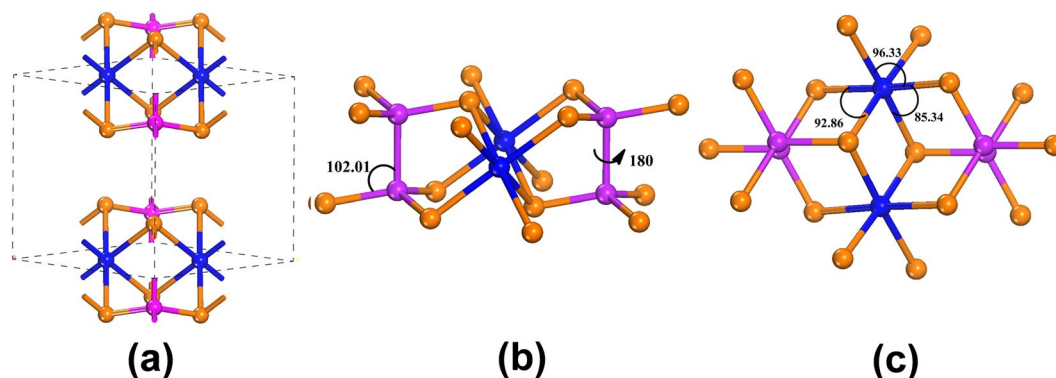
Figure 6. (a) NiPS$_3$ crystal structure showing various atom positions and van der Waals gap. (b) P$_2$S$_6^{4-}$ units showing the dihedral angle of S-P-P-S and the angle of S-P-P. (c) NiS$_6^{10-}$ unit with different bond angles. Blue, pink and brown colours represent nickel, phosphorus and sulphur atoms respectively.

The FET characteristics of transistors and the type of conduction (p- or n-type) will depend on the relative position of the frontier region with respect to the metal contacts. To understand this aspect, the structural modulation of NiPS$_3$ by electron/hole doping has been studied. The parameters obtained for the optimized geometries of neutral and hole/electron doped (0.1e$^-$ per atom) NiPS$_3$ are given in the supporting information (Table S2 and S3 in SI). Same level of theory has been used to perform calculations in all the cases. Doping an electron (0.1e$^-$ per atom) to NiPS$_3$ results in increased (8.01 eV) van der Waals gap and while for hole doping, the gap is found to be reduced (3.20 eV).

Addition of an electron elongates the Ni-S bond length and the opposite effect is observed by hole doping. Very little changes are observed in P-S and P-P bond lengths during electron and hole doping. Further, it is seen that the addition of electron decreases the bond angle distortion in the NiS$_6$ octahedra quite considerably to nearly zero (1.5°) while the hole doping increases the distortion angle by 12° from the neutral value of 26.02°. This suggests that electron doping leads to stable octahedral geometry around Ni. The changes observed in NiS$_6$ units confirm the earlier prediction based on DOS calculations that the doping affects the environment around Ni and S. In the case of electron doping, spin up bands illustrate that the conduction band minimum is observed at G k point and the valance band maximum is found in between L and M k point with a band gap of 1.53 eV while the spin down structure becomes metallic (Fig. 7a). Similarly, the hole doping makes it metallic in nature for spin-up configuration and semiconducting for spin-down configuration (Fig. 7b) with an indirect band gap of 0.47 eV. The results show that NiPS$_3$ changes from semiconducting to metallic nature tuned by electron/hole doping. Magnitude of band gap may also indirectly indicate the stability of materials upon doping. This can be related to the spin flip-gap related stability on doping (Fig. S1).

The atom projected DOS for individual atoms with and without electron/hole doping are shown in Fig. S7. Ni dominates at the Fermi for electron doping while S dominates for hole doping. Interestingly, for electron doped structure, significant increase in the population of Ni is observed near Fermi as compared to neutral NiPS$_3$. It has moved to lower energy region indicating that the structure stabilizes with electron doping. The Ni population decreases near Fermi and minor reduction at the valance band region is observed for the hole doped material. In the case of S, major changes occur only during hole doping. The above results indicate that the electron doping affects Ni and hole doping affects sulphur and consequently the NiS$_6$ unit. This is supported by the lowered bond angle distortions during electron doping thus leading to stable NiS$_6^{10-}$ octahedral environment.

Summary.

The present study has shown the possibilities of fabricating field effect transistors using layered phosphochalcogenides, NiPS$_3$. The FET characteristics show n-type behavior with on/off ratio of 10^3–10^5. The DFT studies have predicted the transport characteristics and are experimentally verified. The phosphochalcogenides with magnetically active centers such as Ni, Co and Mn open ways to flip the spin behavior under magnetic field.

Experimental Section

Synthesis of NiPS$_3$ crystals.

Single crystals of NiPS$_3$ have been synthesized by chemical vapor transport (CVT) technique using iodine as the transporting agent. Pure elements (99.99%) of nickel, phosphorous and sulphur (Aldrich) in stoichiometric proportions with I$_2$ (2 mg/cc) were sealed in an evacuated quartz ampoule. After several attempts, the optimum reaction conditions were arrived at, with hot zone temperature of 950 °C and cold zone of 850 °C that result in high quality, large sized crystals of NiPS$_3$. The schematics of CVT growth setup and the parameters used are given in the supporting information (Fig. S8, S9).

Characterization.

The physicochemical nature of the crystals were identified using X-ray diffraction (XRD) (Philips, PAN analytical, with Cu-Kα radiation), transmission electron microscopy (TEM, JEOL 2100 F operating at 200 kV), Raman spectroscopy (LabRAM, Horiba, France, with excitation wavelength of 514.5 nm and 50x long working distance objective) and atomic force microscopy (AFM, Veeco, NanoscopeIVa Multimode AFM, with silicon nitride, Si$_3$N$_4$ probes of length 130 μm, width 35 μm, resonance frequency, 270 kHz and force
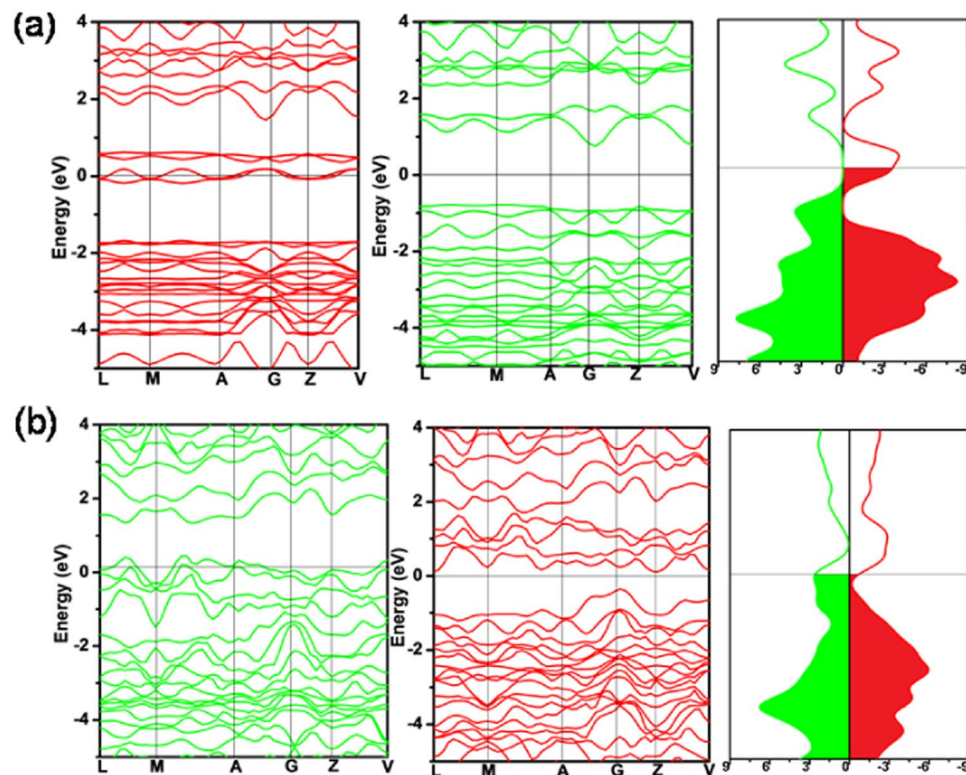
Figure 7. Band structure and total DOS of spin-up (green) and spin-down (red) configurations for (**a**) NiPS$_3$ doped with 0.1 electron per atom, (**b**) NiPS$_3$ doped with 0.1 hole per atom. The Fermi energy is set to zero.

constant, 4.5 N/m). The samples for TEM measurements were prepared by dispersing few-layer NiPS$_3$ colloids onto carbon-coated copper grid and dried under vacuum. The electrical measurements were performed under high vacuum ($<5 \times 10^{-5}$) using Agilent B1500 semiconductor parametric analyzer. Devices were prepared by transferring the material onto pre-fabricated contact pads (Fraunhofer IPMS, Germany) on highly doped silicon with 230 nm SiO$_2$ dielectric using standard mechanical exfoliation method. Source-drain metal contacts were given using 10/60 nm ITO/Au. Highly doped silicon act as the back gate. It was observed that the lithography procedure wherein the sample was exfoliated on Si/SiO$_2$ surface and subsequently depositing the contact pads on the pre-marked areas led to sample deterioration due to the use of solvents during the process.

Computational methodology.   Geometrical optimization calculations for all extended structures has been performed using VASP code[68,69] with plane wave basis truncated at a kinetic energy of 500 eV. The projector augmented wave (PAW) scheme as incorporated in the Vienna ab initio simulation package (VASP) is used in the study (Supporting Information). Density of states and band structure calculations have been performed followed by optimization using CASTEP package[70] including LDA + U approximation. Calculations have been performed for neutral NiPS$_3$ and electron/hole doping separately, and the values are tabulated in Table S1 (Supporting Information).

References

1. Geim, A. K. & Novoselov, K. S. The Rise of Graphene. *Nature Mater.* **6**, 183–191 (2007).
2. Novoselov, K. S. *et al.* Electric Field Effect in Atomically Thin Carbon Films. *Science* **306**, 666–669 (2004).
3. Chhowalla, M. *et al.* The chemistry of two-dimensional layered transition metal dichalcogenide nano sheets. *Nat. Chem.* **5**, 263–275 (2013).
4. Novoselov, K. S. *et al.* Two-dimensional atomic crystals. *Proc. Natl. Acad. Sci.* **102**, 10451–10453 (2005).
5. Radisavljevic, B., Radenovic, A., Brivio, J., Giacometti, V. & Kis, A. Single-layer MoS$_2$ transistors. *Nat. Nanotech.* **6**, 147–150 (2011).
6. Huang, X., Zeng, Z. & Zhang, H. Metal Dichalcogenide Nanosheets: Preparation, Properties and Applications. *Chem. Soc. Rev.* **42**, 1934–1946 (2013).
7. Xu, M., Liang, T., Shi, M. & Chen, H. Graphene-Like Two-Dimensional Materials. *Chem. Rev.* **113**, 3766–3798 (2013).
8. Ross, J. S. *et al.* Electrically tunable excitonic light-emitting diodes based on monolayer WSe$_2$ p-n junctions. *Nat. Nanoteh.* **9**, 268–272 (2014).
9. Baugher, B. W. H., Churchill, H. O. H., Yang, Y. & Herrero, P. J. Optoelectronic devices based on electrically tunable p-n diodes in a monolayer dichalcogenide. *Nat. Nanotech.* **9**, 262–267 (2014).
10. Splendiani, A. *et al.* Emerging Photoluminescence in Monolayer MoS$_2$. *Nano Lett.* **10**, 1271–1275 (2010).
11. Lu, J. *et al.* Improved Photoelectrical Properties of MoS$_2$ Films after Laser Micromachining. *ACS Nano* **8**, 6334–6343 (2014).
12. Pospischil, A., Furchi, M. M. & Mueller, T. Solar-energy conversion and light emission in an atomic monolayer p-n diode. *Nat. Nanotech.* **9**, 257–261 (2014).

13. Kam, K. K.& Parklnclon, B. A. Detailed Photocurrent Spectroscopy of the Semiconducting Group VI Transition Metal Dichaicogenides. *J. Phys. Chem.* **86**, 463-467 (1982).

14. Mak, K. F., Lee, C., Hone, J., Shan, J. & Heinz, T. F. Atomically Thin MoS$_2$: A New Direct-Gap Semiconductor. *Phys. Rev. Lett.* **105**, 136805–136808 (2010).

15. Wang, Q. H., Zadeh, K. K., Kis, A., Coleman, J. N. & Strano, M. S. Electronics and optoelectronics of two-dimensional transition metal dichalcogenides. *Nat. Nanotech.* **7**, 699–712 (2012).

16. Cheng, R. *et al.* Few-layer molybdenum disulfide transistors and circuits for high-speed flexible electronics. *Nat. Commun.* **5**, 5143–5151 (2014).

17. Geim, A. K. & Grigorieva, I. V. Van der Waals heterostructures. *Nature* **499**, 419–425 (2013).

18. Duan, X. *et al.* Lateral epitaxial growth of two-dimensional layered semiconductor heterojunctions. *Nat. Nanotech.* **9**, 1024–1030 (2014).

19. Cheng, R. *et al.* Electroluminescence and Photocurrent Generation from Atomically Sharp WSe$_2$/MoS$_2$ Heterojunction p–n Diodes. *Nano Lett.* **14**, 5590–5597 (2014).

20. Lopez-Sanchez, O., Lembke, D., Kayci, M., Radenovic, A. & Kis, A. Ultrasensitive photodetectors based on monolayer MoS$_2$. *Nat. Nanotech.* **8**, 497–501 (2013).

21. Das, S., Chen, H.-Y., Penumatcha, A. V. & Appenzeller, J. High-Performance Multilayer MoS$_2$ Transistors with Scandium Contacts. *Nano Lett.* **13**, 100–105 (2013).

22. Sarkar, D. *et al.* MoS$_2$ Field-Effect Transistor for Next Generation Label-Free Biosensors. *ACS Nano.* **8**, 3992–4003 (2014).

23. Roy, K. *et al.* Graphene-MoS$_2$ hybrid structures for multifunctional photoresponsive memory devices. *Nat. Nanotech.* **8**, 826–830 (2013).

24. Wang, H. *et al.* Integrated Circuits Based on Bilayer MoS$_2$ Transistors. *Nano Lett.* **12**, 4674–4680 (2012).

25. Fang, H. *et al.* High-Performance Single Layered WSe$_2$ p-FETs with Chemically Doped Contacts. *Nano Lett.* **12**, 3788–3792 (2013).

26. Kou, L., Chen, C. & Smith, S. C. Phosphorene: Fabrication, Properties, and Applications. *J. Phys. Chem. Lett.* **6**, 2794–2805 (2015).

27. Lu, J. *et al.* Bandgap Engineering of Phosphorene by Laser Oxidation toward Functional 2D Materials. *ACS Nano* **9**, 10411–10421 (2015).

28. Abbas, A. N. *et al.* Black Phosphorus Gas Sensors. *ACS Nano* **9**, 5618–5624 (2015).

29. Li, L. *et al.* Black phosphorus field-effect transistors. *Nat. Nanotechn.* **9**, 372–377 (2014).

30. Das, S., Demarteau, M. & Roelofs, A. Ambipolar Phosphorene Field Effect Transistor. *ACS Nano* **8**, 11730–11738 (2014).

31. Lacroix, P. G., Clement, R., Nakatani, K., Zyss, J. & Ledoux, I. Stilbazolium-MPS$_3$ Nanocomposites with Large Second-Order Optical Nonlinearity and Permanent Magnetization. *Science* **263**, 658–660 (1994).

32. Evans, J. S. O. & O'hure, D. Kinetics of the Intercalation of Cations into MnPS$_3$, Using Real Time *In Situ* X-Ray Diffraction. *Adv. Mater.* **6**, 646–648 (1994).

33. Leflem, G., Brec, R., Ouvard, G., Louisy, A. & Segransan, P. Magnetic-interactions in the layer compounds MPX$_3$ (M = Mn, Fe, Ni; X = S, Se). *J. Phys. Chem. Solids* **43**, 455–461 (1982).

34. Clement, R., Girerd, J. J. & Morgenstern-badarau, I. Dramatic modification of the magnetic properties of lamellar MnPS$_3$ upon intercalation. *Inorg. Chem.* **19**, 2852–2854 (1980).

35. Joy, P. A. & Vasudevan, S. Magnetism in the layered transition-metal thiophosphates MPS$_3$ (M = Mn, Fe, and Ni). *Phys. Rev. B.* **46**, 5425–5433 (1992).

36. Evans, J. S. O., Ohare, D., Clement, R., Leaustic, A. & Thuery, P. Origins of the spontaneous magnetization in MnPS$_3$ intercalates-a magnetic-susceptibility and powder neutron diffraction study. *Adv. Mater.* **207**, 735–739 (1995).

37. Li, X., Wu, X. & Yang, J. Half-metallicity in MnPSe$_3$ exfoliated nanosheet with carrier doping. *J. Am. Chem. Soc.* **136**, 11065–11069 (2014).

38. Rule, K. C., McIntyre, G. J., Kennedy, S. J. & Hicks, T. J. Single-crystal and powder neutron diffraction experiments on FePS$_3$: search for the magnetic structure. *Phys. Rev. B* **76**, 134402–134408 (2007).

39. Leaustic, A. *et al.* Constant-Machado H. High-T-c magnets in a series of substituted pyridinium–FePS$_3$ layered intercalates. *Chem. Mater.* **8**, 1954–1961 (1996).

40. Kuo, C.-T. *et al.* Exfoliation and Raman Spectroscopic Fingerprint of Few-Layer NiPS$_3$ van der Waals Crystals. *Sci. Rep.* **6**, 20904–20913 (2015).

41. Du, K.-Z. *et al.* Weak Van der Waals Stacking, Wide-Range Band Gap, and Raman Study on Ultrathin Layers of Metal Phosphorus Trichalcogenides. *ACS Nano* **10**, 1738–1743 (2016).

42. Long, G. *et al.* Isolation and Characterization of Few-Layer Manganese Thiophosphite. *ACS Nano* **11**, 11330–11336 (2017).

43. Jenjeti, R. N., Austeria, P. M. & Sampath, S. Alternate to Molybdenum Disulfide: A 2D, Few-Layer Transition-Metal Thiophosphate and Its Hydrogen Evolution Reaction Activity over a Wide pH Range. *ChemElectroChem* **3**, 1392–1399 (2016).

44. Li, K., Rakov, D., Zhang, W. & Xu, P. Improving the intrinsic electro catalytic hydrogen evolution activity of few-layer NiPS$_3$ by cobalt doping. *Chem. Commun.* **53**, 8199–8202 (2017).

45. Mukherjee, D., Austeria, P. M. & Sampath, S. Two-Dimensional, Few-Layer Phosphochalcogenide, FePS$_3$: A New Catalyst for Electrochemical Hydrogen Evolution over Wide pH Range. *ACS Energy Lett.* **1**, 367–372 (2016).

46. Konkena, B. *et al.* Metallic NiPS$_3$@NiOOH Core–Shell Heterostructures as Highly Efficient and Stable Electrocatalyst for the Oxygen Evolution Reaction. *ACS Catal.* **7**, 229–237 (2017).

47. Wang, F. *et al.* Two-dimensional Metal Phosphorus Trisulfide Nanosheet with Solar Hydrogen-Evolving Activity. *Nano Energy* **40**, 673–680 (2017).

48. Chu, J. *et al.* High-Performance Ultraviolet Photodetector Based on a Few-Layered 2D NiPS$_3$ Nanosheet. *Adv. Funct. Mater.* **27**, 1701342 (2017).

49. Susner, M. A., Chyasnavichyus, M., McGuire, M. A., Ganesh, P. & Maksymovych, P. Metal Thio- and Selenophosphates as Multifunctional van der Waals Layered Materials. *Adv. Mater.* 1602852−1602891 (2017).

50. Zhang, X., Zhao, X., Wu, D., Jing, Y. & Zhou, Z. MnPSe$_3$ Monolayer: A Promising 2D Visible-Light Photohydrolytic Catalyst with High Carrier Mobility. *Adv. Sci.* 1600062-1600066 (2016).

51. Brec, R. Review on structural and chemical properties of transition metal phosphorus trisulfides MPS$_3$. *Solid State Ionics* **22**, 3–30 (1986).

52. Berasconi, M., Marra, G. L., Benedek, G. & Miglio, L. Lattice dynamics of layered MPX$_3$ (M = Mn, Fe, Ni, Zn; X = S, Se) compounds. *Phy. Rev.* **B38**, 12089–12099 (1998).

53. El-Mahalawy, S. H. & Evans, B. L. Temperature dependence of the electrical conductivity and hall coefficient in 2H-MoS$_2$, MoSe$_2$, WSe$_2$, and MoTe$_2$. *Phys. Stat. Sol. (b)* **79**, 713–722 (1997).

54. Huang, Y. *et al.* Reliable Exfoliation of Large-Area High-Quality Flakes of Graphene and Other Two-Dimensional Materials. *ACS Nano* **9**, 10612–10620 (2015).

55. Feng, Q. *et al.* Growth of Large-Area 2D MoS$_{2(1−x)}$Se$_{2x}$ Semiconductor Alloys. *Adv. Mater.* **26**, 2648–2653 (2014).

56. Huang, J. *et al.* Large-area Synthesis of Monolayer WSe$_2$ on SiO$_2$/Si Substrate and its Device Applications. *Nanoscale* **7**, 4193–4198 (2015).

57. Zhang, Y. *et al.* Thickness Considerations of Two-Dimensional Layered Semiconductors for Transistor Applications. *Sci. Rep.* **6**, 29615–29621 (2016).

58. Piacentini, M., Khumalo, F. S., Olson, C. G., Anderegg, J. W. & Lych, D. W. Optical transitions, XPS and electronic states in NiPS₃. *Chem. Phy* **65**, 289–304 (1982).
59. Foot, P. J. S., Suradi, J. & Lee, P. A. Optical and electronic properties of the layered semiconductors NiPS₃ and FePS₃. *Mat. Res. Bull.* **15**, 189–193 (1980).
60. Foot, P. J. S. *et al.* The Structures and Conduction Mechanisms of Lithium-Intercalated and Lithium-Substituted Nickel Phosphorus Trisulphide (NiPS₃), and the Use of the Material as a Secondary Battery Electrode. *Phys. stat. sol. (a)* **100**, 11–29 (1987).
61. Chen, J.-R. *et al.* Control of Schottky Barriers in Single Layer MoS₂ Transistors with Ferromagnetic Contacts. *Nano Lett.* **13**, 3106–3110 (2013).
62. Kim, S. *et al.* High-mobility and low-power thin-film transistors based on multilayer MoS₂ crystals. *Nat. Commun.* **3**, 1011–1017 (2012).
63. Li, S.-L. *et al.* Thickness-Dependent Interfacial Coulomb Scattering in Atomically Thin Field-Effect Transistors. *Nano Lett.* **13**, 3546–3552 (2013).
64. Alegria, E. C. B. A. *et al.* Mono-alkylation of cyanoimide at a molybdenum(IV) diphosphinic center by alkyl halides: synthesis, cathodically induced isomerization and theoretical studies. *Electrochim. Acta* **218**, 252–262 (2016).
65. Ertl, A. *et al. Polyhedron distortions in tourmaline.* **40**, 153–162 (2012).
66. Fop, S., Wildman, E. J., Skakle, J. M. S., Ritter, C. & McLaughlin, A. C. Electrical and Structural Characterization of Ba₃Mo₁₋ₓNb₁₊ₓO₈.₅₋ₓ/₂: The Relationship between Mixed Coordination, Polyhedral Distortion and the Ionic Conductivity of Ba₃MoNbO₈.₅. *Inorg. Chem.* **56**, 10505–10512 (2017).
67. Robinson, K., Gibbs, G. V. & Ribbe, P. H. Quadratic Elongation: A Quantitative Measure of Distortion in Coordination Polyhedra. *Science* **172**, 567–570 (1971).
68. Kresse, G. & Hafner, J. *Ab initio* molecular dynamics for liquid metals. *Phys. Rev. B* **47**, 558–561 (1993).
69. Kresse, G. & Hafner, J. *Ab initio* molecular-dynamics simulation of the liquid-metal–amorphous-semiconductor transition in germanium. *Phys. Rev. B* **49**, 14251–14269 (1994).
70. Segall, M. D. *et al.* First-principles simulation: ideas, illustrations and the CASTEP code. *Journal of Physics: Conden. Mat.* **14**(11), 2717–2744 (2012).

Acknowledgements

Author Contributions

Ramesh Naidu Jenjeti synthesized the material and carried out FET studies. Rajat Kumar helped in carrying out certain transport measurements while Muthu P. Austeria carried out computational studies. S. Sampath conceived the research problem and all authors contributed in the interpretation of data and writing the manuscript.

Additional Information

Supplementary information accompanies this paper at https://doi.org/10.1038/s41598-018-26522-1.

Competing Interests: The authors declare no competing interests.

Publisher's note: Springer Nature remains neutral with regard to jurisdictional claims in published maps and institutional affiliations.